Dept. of Math. University of Oslo
Mechanics and Applied Mathematics No. 2
ISSN 0809–4403 August 2008

Influence of cross channel depth variation on ship wave patterns

T. Torsvik[3], G. Pedersen[2] and K. Dysthe[1]
[1] Department of Mathematics, University of Bergen,
Johannes Brunsg. 12, N-5008 Bergen, Norway
[2] Department of Mathematics, University of Oslo, PO box 1053, 0316 Oslo, Norway
[3] Bergen Center for Computational Science, University of Bergen,
Høyteknologisenteret, Thormøhlensgate 55, N-5008 Bergen, Norway

August 5, 2008

Abstract

The present work is a numerical investigation on waves generated by a pressure disturbance moving at constant speed in a channel with a variable cross-channel depth profile. The channel profile, which is uniform in the along-channel direction, has a deep trench located in the vicinity of the center line of the channel, and shallow banks near the channel walls. Wave fields generated upstream and downstream of the moving pressure disturbance are described, and the characteristic features present in the wave patterns are related to the parameters governing the speed of the pressure disturbance and the shape of the cross-channel profile. Our numerical investigation is based on the COULWAVE long wave model, which solves a set of Boussinesq type equations in two horizontal dimensions.

1 Introduction

In coastal waters, ships are often required to navigate in natural or dredged trenches. Long waves are known to be generated by high speed vessels traveling at speeds close to the critical depth Froude number

$$F = \frac{U}{\sqrt{gh}} = 1 \tag{1}$$

where U is the speed of the vessel, g is the acceleration of gravity and h is the depth. In order to examine how ship waves behave under these conditions, we consider the idealized case where waves, generated by a moving pressure disturbance, propagate in a channel with a deep trench at the centre line and shallow banks along the channel walls. We are particularly interested in cases where the speed of the pressure disturbance is subcritical with respect to the Froude number in the trench, but near critical or supercritical with respect to the shallow banks. Because the ship wave pattern changes substantially in the transition between the subcritical and supercritical regime, these test may provide us with a better understanding on how the different features in the bathymetry influences the wave pattern.

Several researchers have studied waves propagating in channels with arbitrary cross-section profiles[19, 18] and the wave patterns, in two horizontal dimensions (2HD), generated by a

disturbance moving at speeds close to the critical Froude number in channels with a rectangular cross-section profile[1, 3, 17]. Mathew and Akylas[12] brought these elements together in their study of waves propagating in channels with a trapezoidal cross-section profile. Recently, Teng and Wu[24], Jiang et al.[2], and Liu and Wu[6] have made contributions to this field of research. Most of these studies deal with channels with trapezoidal cross-section profiles, but Jiang et al.[2] also include results for a channel with a deep trench along the center line, which is similar to the cases that will be discussed in this paper.

In our study, we simulate the wave generation and propagation using COULWAVE, a computer model for long waves, developed at Cornell University by Lynett, Wu and Liu[8, 10, 7]. The model is based on a set of weakly dispersive, fully nonlinear Boussinesq equations, first developed by Liu[5] and Wei et al.[25]. A version of the model which includes a pressure disturbance has been implemented by Liu and Wu[6].

2 Mathematical model equations

The numerical model is based on a set of fully nonlinear and weakly dispersive Boussinesq equations, which are nondimensionalized by introducing the characteristic depth h_0, as the length scale, $\sqrt{g/h_0}$ as the time scale, and the hydrostatic pressure $\rho g h_0$, as the pressure scale. In dimensionless form, the Boussinesq equations consist of the continuity equation

$$\begin{aligned}
&\frac{\partial \zeta}{\partial t} + \nabla \cdot [(\zeta + h)\mathbf{u}_\alpha] \\
&\quad + \nabla \cdot \left\{ \left(\frac{z_\alpha^2}{2} - \frac{h^2}{6} \right) h \nabla (\nabla \cdot \mathbf{u}_\alpha) + \left(z_\alpha + \frac{h}{2} \right) h \nabla [\nabla \cdot (h\mathbf{u}_\alpha)] \right\} \\
&\quad + \nabla \cdot \left\{ \zeta \left[\left(z_\alpha - \frac{1}{2}\zeta \right) \nabla (\nabla \cdot (h\mathbf{u}_\alpha)) + \frac{1}{2} \left(z_\alpha^2 - \frac{1}{3}\zeta^2 \right) \nabla (\nabla \cdot \mathbf{u}_\alpha) \right] \right\} \\
&\quad = 0 \,,
\end{aligned} \tag{2}$$

and the momentum equation

$$\begin{aligned}
&\frac{\partial \mathbf{u}_\alpha}{\partial t} + (\mathbf{u}_\alpha \cdot \nabla)\mathbf{u}_\alpha + \nabla \zeta + \nabla p \\
&\quad + \left\{ \nabla \left[z_\alpha \left(\nabla \cdot \left(h \frac{\partial \mathbf{u}_\alpha}{\partial t} \right) \right) \right] + \nabla \left[\frac{1}{2} z_\alpha^2 \left(\nabla \cdot \frac{\partial \mathbf{u}_\alpha}{\partial t} \right) \right] \right\} \\
&\quad + \nabla \left\{ \frac{1}{2} z_\alpha^2 \mathbf{u}_\alpha \cdot \nabla (\nabla \cdot \mathbf{u}_\alpha) + z_\alpha \mathbf{u}_\alpha \cdot \nabla (\nabla \cdot h\mathbf{u}_\alpha) \right. \\
&\quad \left. + \frac{1}{2} [\nabla \cdot (h\mathbf{u}_\alpha)]^2 - \zeta \nabla \cdot \left(h \frac{\partial \mathbf{u}_\alpha}{\partial t} \right) \right\} \\
&\quad + \nabla \left\{ \zeta (\nabla \cdot h\mathbf{u}_\alpha)(\nabla \cdot \mathbf{u}_\alpha) - \frac{1}{2} \zeta^2 \nabla \cdot \left(\frac{\partial \mathbf{u}_\alpha}{\partial t} \right) - \zeta \mathbf{u}_\alpha \cdot \nabla (\nabla \cdot h\mathbf{u}_\alpha) \right\} \\
&\quad + \nabla \left\{ \frac{1}{2} \zeta^2 (\nabla \cdot \mathbf{u}_\alpha)^2 - \frac{1}{2} \zeta^2 \mathbf{u}_\alpha \cdot \nabla (\nabla \cdot \mathbf{u}_\alpha) \right\} = 0 \,,
\end{aligned} \tag{3}$$

where $\zeta(x, y, t)$ is the surface displacement, $\mathbf{u}_\alpha(x, y, t) = (u_\alpha(x, y, t), v_\alpha(x, y, t))$ is the velocity at the depth $z = z_\alpha$, $\nabla = (\partial/\partial x, \partial/\partial y)$ is the horizontal gradient operator, ρ is the density of water and $p(x, y, t)$ is the pressure disturbance of magnitude p_a at the free surface. The reference

depth $z_\alpha = -0.531h$ is applied, following the recommendation by Nwogu[16]. This optimizes the dispersive properties of the equations with respect to the linear dispersion relation over a range of long and intermediate waves. With the model equations formulated as above, wave propagation in terms of phase velocity and group velocity is accurately described for waves with dimensionless wave number in the range $0 < kh \leq \pi$, as shown by Madsen and Schäffer[11].

When deriving (2) and (3), it is assumed that the characteristic water depth h_0, is small relative to the horizontal length scale λ, i.e. $\mu = h_0/\lambda \ll 1$. The characteristic wave amplitude a may be of the same order of magnitude as h_0, and the nonlinear effects, related to the parameter $\epsilon = a/h_0 = O(1)$ are not required to be weak. The model equations (2) and (3) are accurate up to $O(\mu^2)$.

In our simulations we represent a monohull vessel by a localized pressure disturbance (see e.g. [1, 3, 17, 4]). Waves generated by a thin ship representation was also examined in [17] and [4], where the ship is represented by a slender body extending from the free surface down to the sea bed. These studies showed that the different wave generating mechanisms generated qualitatively similar wave patterns, although the waves generated by a pressure disturbance were generally smoother than waves generated using the thin ship representation. In our study we are not concerned about waves generated by a ship with a particular hull shape, and in this case the pressure disturbance representation is adequate.

The forcing pressure disturbance is defined according to

$$p(x + Ft, y) = p_a f(x + Ft) q(y)\,,$$

where the Froude number F is defined according to eq. (1). Functions f and q are defined by

$$f(x + Ft) = \cos^2\left[\frac{\pi(x + Ft)}{2L}\right]\,, \quad -L \leq x + Ft \leq L\,,$$

$$q(y) = \cos^2\left(\frac{\pi y}{2R}\right)\,, \quad -R \leq y \leq R\,,$$

on $-L \leq x + Ft \leq L$, $-R \leq y \leq R$, and is zero outside this rectangle. Typical values for the pressure disturbance is $p_a = 0.1$, $L = 4.0h_0$, and $R = 2.0h_0$. In the following figures, the pressure disturbance moves towards decreasing values of x, and the along-channel coordinate is redefined as

$$\xi = x + Ft\,,$$

in which the location of the pressure disturbance remains fixed at all times. In this frame of reference, upstream waves are located to the left of the pressure disturbance. At the start of the simulation, the pressure disturbance is abruptly set in motion at a particular speed, which is maintained constant thereafter.

Numerical method

The COULWAVE model applies an algorithm which is similar to the method of Wei et al.[25]. The algorithm is formally accurate to Δt^4 in time. The first-order spatial derivatives in the equations are discretized to fourth order, whereas the spatial derivatives in the dispersive terms are discretized to second order. This ensures that the numerical dispersion related to the spatial derivatives of first order is of higher order than the physical dispersive terms. The algorithm

is marched forward in time using the Adams-Bashforth-Moulton predictor-corrector scheme to update the dependent variables.

Although the algorithm is formally of second order in space, this convergence rate has not been achieved in the simulations. The numerical results converge when the grid resolution is increased, but the convergence is slow for the steep, large amplitude waves often found immediately downstream of the pressure disturbance. A five point filter has been applied to avoid saw-tooth noise which tends to emerge in the cross-channel direction. A small damping is also inherent in the time stepping scheme. No other dissipative terms have been added to smooth the variable fields. The model has been tested by running the same simulation with spatial grid resolutions of $0.1\,h_0$, $0.2\,h_0$, and $0.4\,h_0$. Using the finest resolution as reference, we calculated the relative errors E_u and E_d, for the amplitudes of the leading upstream wave and the first downstream wave, respectively. For $\Delta x = \Delta y = 0.4\,h_0$, the errors $E_u = 2.0 \cdot 10^{-2}$ and $E_d = 2.5 \cdot 10^{-1}$ were found, while increasing the grid resolution to $\Delta x = \Delta y = 0.2\,h_0$, reduced the errors to $E_u = 4.5 \cdot 10^{-3}$ and $E_d = 7.1 \cdot 10^{-2}$. A spatial grid resolution of $\Delta x = \Delta y = 0.2\,h_0$ has been used for all subsequent simulations in this paper.

The pressure disturbance is often required to travel a length of order $O(10^3 h_0)$ for the wave pattern to fully develop. In order to speed up the computation, the wave field is only computed in a window including the parts of the channel immediately upstream and downstream of the pressure disturbance. This window is shifted upstream when the free surface displacement grows to $\delta = 0.05\,p_a$ somewhere along a cross-channel line located $30\,h_0$ downstream of the upstream boundary. A potential problem with this method is contamination from waves generated at the downstream boundary, which is of particular concern for simulations where the Froude number is subcritical. By running the same simulation with different sizes of computational windows, we found that by the end of the simulation, the error was $O(10^{-8})$ at $50\,h_0$ downstream of the pressure disturbance, and $O(10^{-3})$ near the downstream boundary of the smallest computational window, located $88.5\,h_0$ downstream of the pressure disturbance. We also tested for the sensitivity to the shifting criteria by running the model with $\delta = 0.01\,p_a$. The errors were found to be $O(10^{-5})$ everywhere, except near the downstream boundary.

3 Results

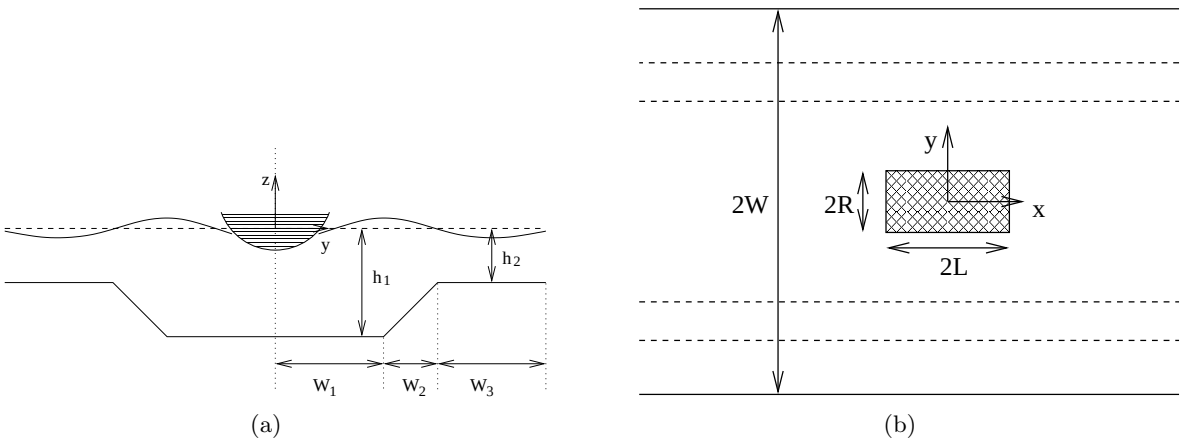

Figure 1: Channel cross-sectional profile, and sketch of the pressure disturbance.

In this section we present results based on numerical simulations where waves are generated by a moving pressure disturbance in a channel with a variable cross-channel topography. The channel has a deep section along the center line and shallow banks near the solid boundaries. The parameters for the cross-channel variation are defined according to Fig. 1. We will refer to the depth at the center line as h_1, and the depth at the channel wall as h_2. The total width of the channel is $2W$, but because the wave pattern is symmetrical across the line $y = 0$, we run the simulations only on the half plane $0 \leq y \leq W$. The widths of the different regions are given by the triplet $W = (W_1, W_2, W_3)$, where W_1 is the half-width of the trench, W_2 is the width of the sloping region, and W_3 is the width of the shallow bank adjacent to the channel wall. This cross-channel profile is similar to one of the examples discussed by Jiang et al.[2]. A direct comparison between our results and the result presented in Jiang et al.[2] has not been attempted, because Jiang et al. do not quantify the free surface displacement attained in their simulation.

3.1 Influence of the Froude number on the wave pattern

In this part we examine how the wave pattern is influenced by changing the velocity of the advancing pressure disturbance. The channel is defined by $W = (3, 2, 5)$, $h_1 = 1.0$ and $h_2 = 0.6$, and the velocities used in the simulations corresponds to Froude numbers at the trench of $F_1 = 0.7$, 0.8, 0.9 and 1.0, which give Froude numbers $F_2 = 0.9037$, 1.0328, 1.1619 and 1.2910, respectively, at the shallow banks. Figure 2 shows contour plots of the generated waves at $t = 1253$, figure 3 shows the leading downstream waves in greater detail, and figure 4 shows along-channel wave profiles at $y = 0$, 5 and 10.

For $F_1 = 0.7$ and $F_2 = 0.9037$, the upstream wave generation, shown if Figs. 2(a) and 4(a), seems to be transient in nature, and depends on the startup of the simulation (see discussion in section 3.5). In the region immediately upstream of the pressure disturbance, both the wave amplitude and the mean surface elevation tend to zero with time. A steady state is attained downstream of the pressure disturbance, shown in figure 3(a), where the wave pattern consists of small amplitude waves with wave lengths of $\lambda \approx 3$. Since $hk \approx 2$ is within the range where the wave dispersion is accurately described, we can expect the results to be reasonable even for these short waves. This is a case which clearly demonstrates the advantage of using Boussinesq models with improved dispersion properties instead of the standard form of the Boussinesq equations.

The leading part of the upstream wave in figure 4(a) resembles the Airy function $Ai(\xi)$, which is the traveling wave solution for the linearized equations. These waves display only a slight cross-channel variation in amplitude and no cross-channel variation in phase speed despite the significant cross-channel variation in depth. It may seem strange that an essentially linear waves should not be influenced by the depth variation. In this case the leading waves are long not only with respect to the depth, but also with respect to the width of the channel, and is therefore only influenced by the mean depth in the channel. This is also consistent with the fact that the cross-channel variation increases as the wave length decreases in the wave train.

When the Froude number is increased to $F_1 = 0.8$ and $F_2 = 1.0328$, an undular bore is generated upstream of the moving pressure disturbance, as seen in Figs. 2(b) and 4(b). We note that the wave crests of the upstream waves span the channel at an angle which is nearly perpendicular to the channel wall, and that the amplitude, although higher at the wall than at the center of the channel, varies only slightly in the cross-channel direction. Waves with large amplitudes are generated downstream of the pressure field for $F_1 = 0.8$. These high amplitudes

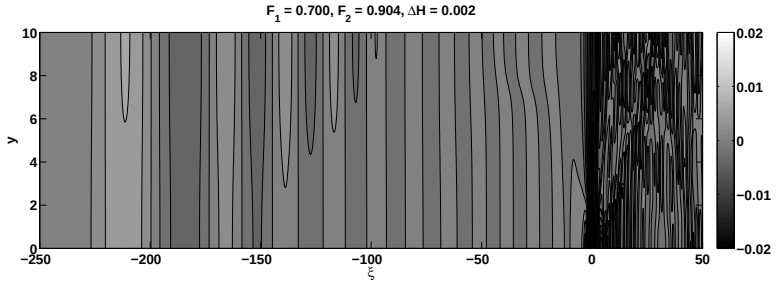

(a)

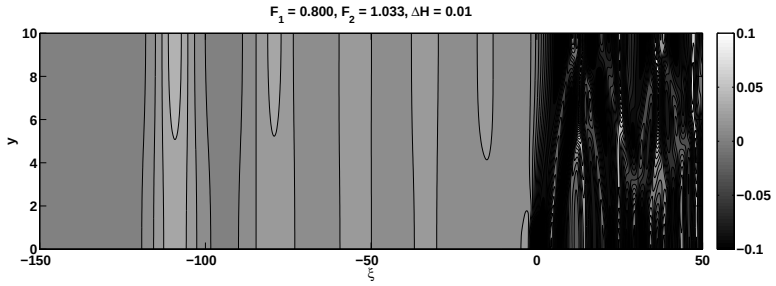

(b)

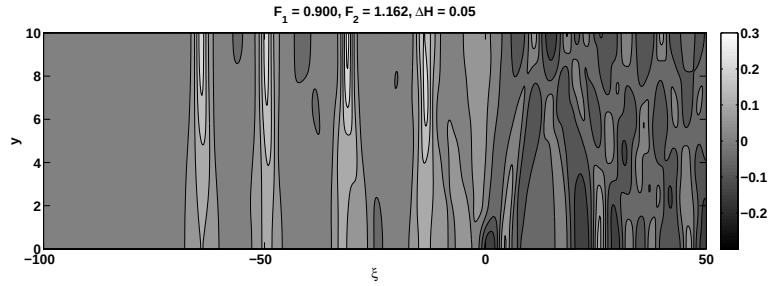

(c)

Figure 2: Contour plot of waves generated at different Froude numbers. Contour levels given by ΔH for each plot.

occur near the channel wall ($y = 10$) due to wave reflection at the solid boundary, but also in the shallow part of the channel ($5 < y < 8$) due to wave-wave interaction.

While the waves generated for $F_1 = 0.7$ and $F_1 = 0.8$ clearly conforms to subcritical wave patterns, the wave pattern generated at $F_1 = 0.9$ and $F_2 = 1.1619$, seen in Figs. 2(c) and 4(c), shows what appears to be a persistent generation of upstream waves which is characteristic for the near critical wave pattern. It is notable that this wave pattern occurs when the local Froude number at the trench is still subcritical. The leading upstream wave attains the bell-shaped form often associated with solitary waves, but is trailed by small amplitude disturbances which interact with the following upstream waves. Diffraction of the leading upstream wave due to depth variation has also been reported by [12], who studied the propagation of an undular bore in a trapezoidal channel. The wave diffraction due to depth variation is more prominent in the middle of the channel than at the channel walls, as seen in Fig. 4(c). Even though wave diffraction occurs, causing significant variation in amplitude and wave profiles in the cross-

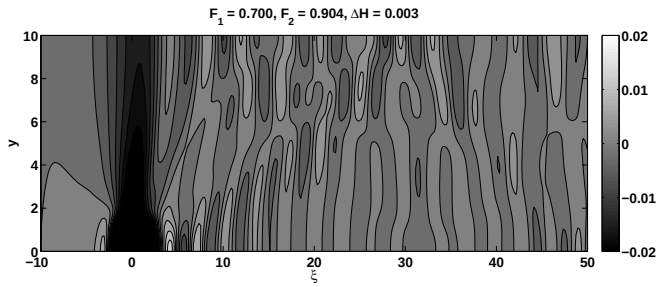

(a)

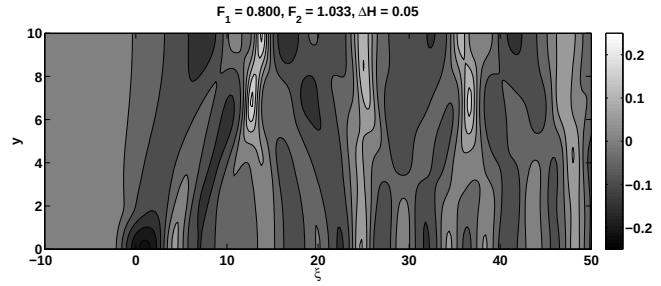

(b)

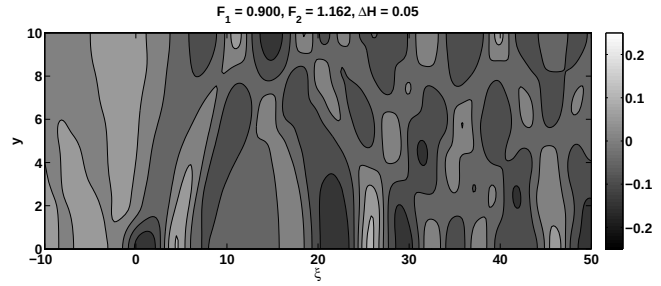

(c)

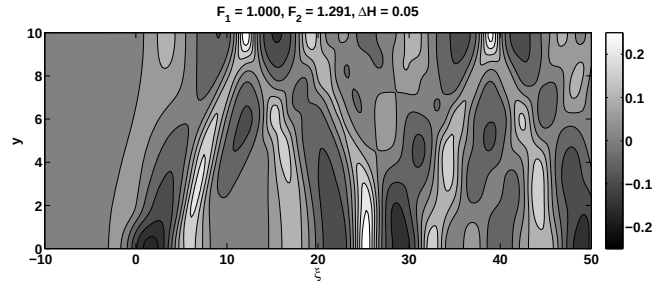

(d)

Figure 3: Details of the downstream wave pattern. Contour levels given by ΔH for each plot.

channel direction, each of the upstream waves can be clearly identified as distinct waves with wave crests oriented nearly perpendicular to the channel wall. The amplitudes of the downstream waves for $F_1 = 0.9$, seen in Fig. 3(c), are of the same order of magnitude as for $F_1 = 0.8$, and the largest peaks are located near the center line of the channel and near the channel walls.

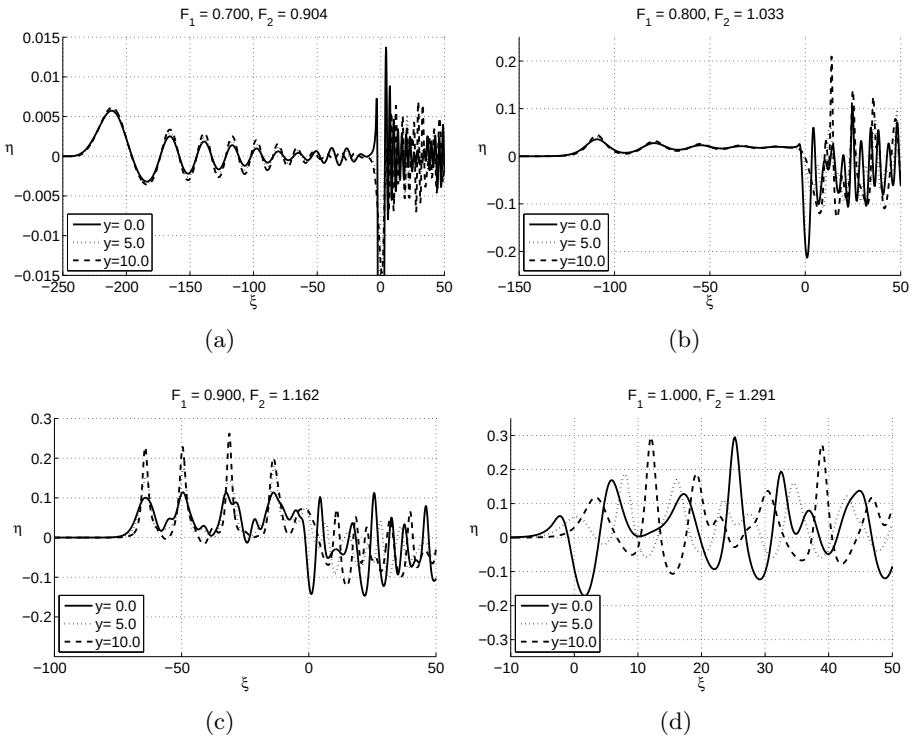

Figure 4: Wave cuts along the channel of the wave patterns shown in Fig. 2.

Waves do not propagate upstream of the pressure field for $F_1 = 1.0$ ($F_2 = 1.2910$), so the wave pattern consists only of the downstream waves, as seen in Fig. 3(d). Although the reflection of the leading wave at the wall resembles the stem seen in Mach reflection (see e.g. [15]), this is not a feature of Mach reflection because the stem does not grow with time and the wave does not propagate upstream relative to the pressure disturbance. The lack of upstream waves for $F_1 = 1.0$ may seem to contradict results from previous studies. We return to this point in the discussions at the end of the paper. Due to the lack of upstream wave generation, all the wave energy is transferred downstream of the pressure field. Hence the wave amplitude of downstream waves are seen to be significantly larger than for $F_1 = 0.9$, particularly where the waves amplify near the channel wall and the center line of the channel.

3.2 Waves radiated upstream of the pressure field

For $F_1 = 0.8$, the upstream waves propagate as an undular bore. The position of the leading wave crest $\xi_w(y,t)$ is plotted in figure 5(a), for $y = 0$, 5, and 10. Early in the simulation, the position of the leading wave is located further upstream at the center of the channel than at the channel walls. While the wave crest at the center line initially remains nearly stationary compared to the position of the pressure disturbance, with $\xi_w(0,t) = -3.3 \pm 0.1$, the wave crest at the channel wall is seen to propagate upstream. The straightening of the wave crest at the channel wall and the upstream propagation is clearly a feature of Mach reflection, which was previously found by Pedersen[17] to occur for waves generated in channels with a rectangular cross-channel profile.

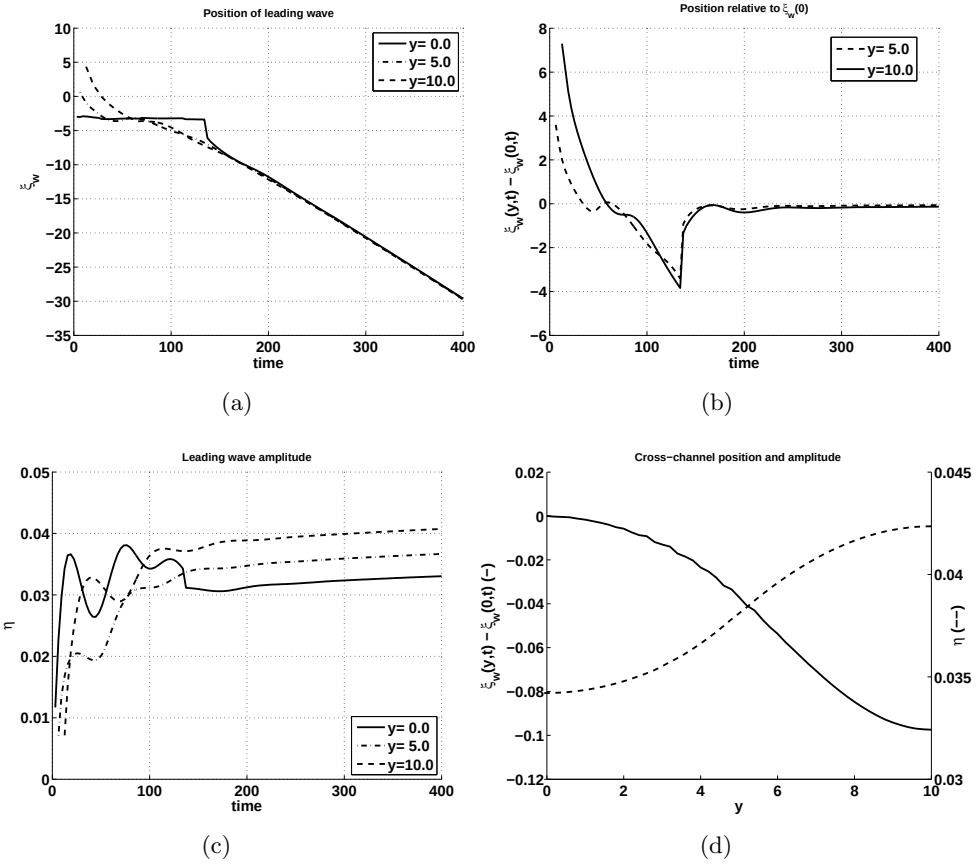

Figure 5: Position and amplitude of the leading upstream wave for $F_1 = 0.8$.

The wave propagation at the wall slows down at $t \approx 75$, when the wave crest has become nearly a straight line, as seen in figure 5(b), where the position of the wave crest $\xi_w(y,t)$ is plotted relative to $\xi_w(0,t)$. This coincides with a temporary slump in the wave amplitude at the wall, as seen in figure 5(c). Once the wave amplitude at the wall increases, the waves crest over the shallow bank propagate a considerable distance upstream of the crest at the center line, before an abrupt adjustment occurs at $t \approx 135$, which brings the wave crest at the center line into alignment with the wave crest near the channel wall. From figure 5(a) it is apparent that the adjustment shifts the central part of the upstream wave forward to the position of the wave near the channel wall. After the adjustment, the leading wave propagate with a constant speed c_w of approximately $c_w/U = 1.12$, which is subcritical ($c_w/\sqrt{h_1} = 0.89$) at $y = 0$ and supercritical ($c_w/\sqrt{h_2} = 1.15$) at $y = 10$. The cross-channel amplitude increases from the center line to the channel wall, as shown by the stapled line in figure 5(d), and the mean wave amplitude is increasing slowly with time, as seen in figure 5(c). This may however be a transient phenomenon, because the upstream waves form an undular bore which is not fully developed within the time shown, which means that wave energy is still transfered to the leading wave from the rear. The wave crest is located slightly further upstream near the channel wall than the center line, as seen by the solid line in figure 5(d).

The generation of the leading upstream wave for $F_1 = 0.9$ follow much the same pattern

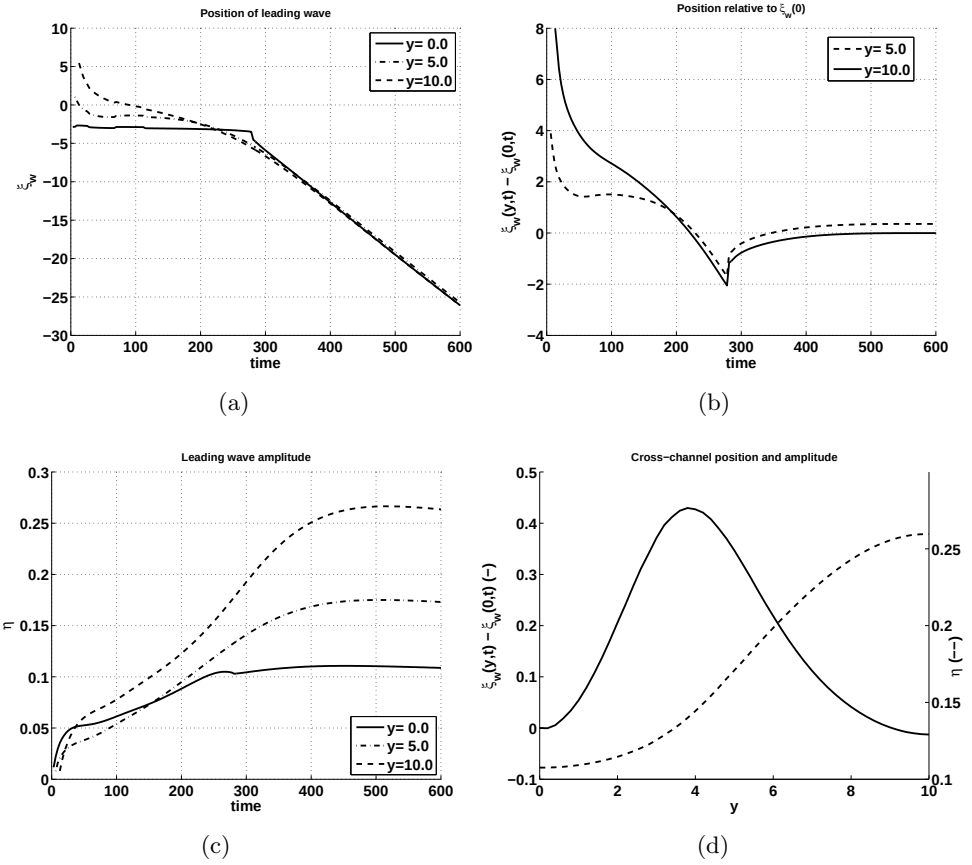

Figure 6: Position and amplitude of the leading upstream wave for $F_1 = 0.9$.

as for $F_1 = 0.8$. At the start of the simulation, the upstream crest at $y = 0$ is stationary at $\xi_w(0,t) = -3.2 \pm 0.3$, but adjusts to the wave crest in the far field at $t \approx 280$, as seen in Fig. 6(a). The wave crest is located nearly the same distance upstream near the center line and near the channel wall, but lags behind by $0.4h_0$ at $y = 4$, as seen in figure 6(d). The wave amplitude decreases with time, as seen in figure 6(c), which is to be expected because the wave is subject to wave diffraction. The wave propagates at approximately $c_w/U = 1.07$, which is subcritical ($c_w/\sqrt{h_1} = 0.96$) at $y = 0$ and supercritical ($c_w/\sqrt{h_2} = 1.25$) at $y = 10$.

3.2.1 Comparison with cross-channel averaged theory

For the channel configurations used in the examples above, we often find that the leading upstream wave is long compared to the width of the channel. These results may therefor be comparable to results using cross-channel averaged models, which were first developed by Peters[19] and Peregrine[18], and have more recently been applied by Teng and Wu[22]. The models are based on weakly nonlinear and dispersive equations, such as KdV and standard Boussinesq equations, and are developed under the assumption that the cross-channel variation of the velocity and wave amplitude is small compared to the along-channel variation. Under these conditions, it is possible to determine the solitary wave solution analytically, given a mean wave amplitude and a specific cross-channel depth profile. The procedure is briefly outlined in

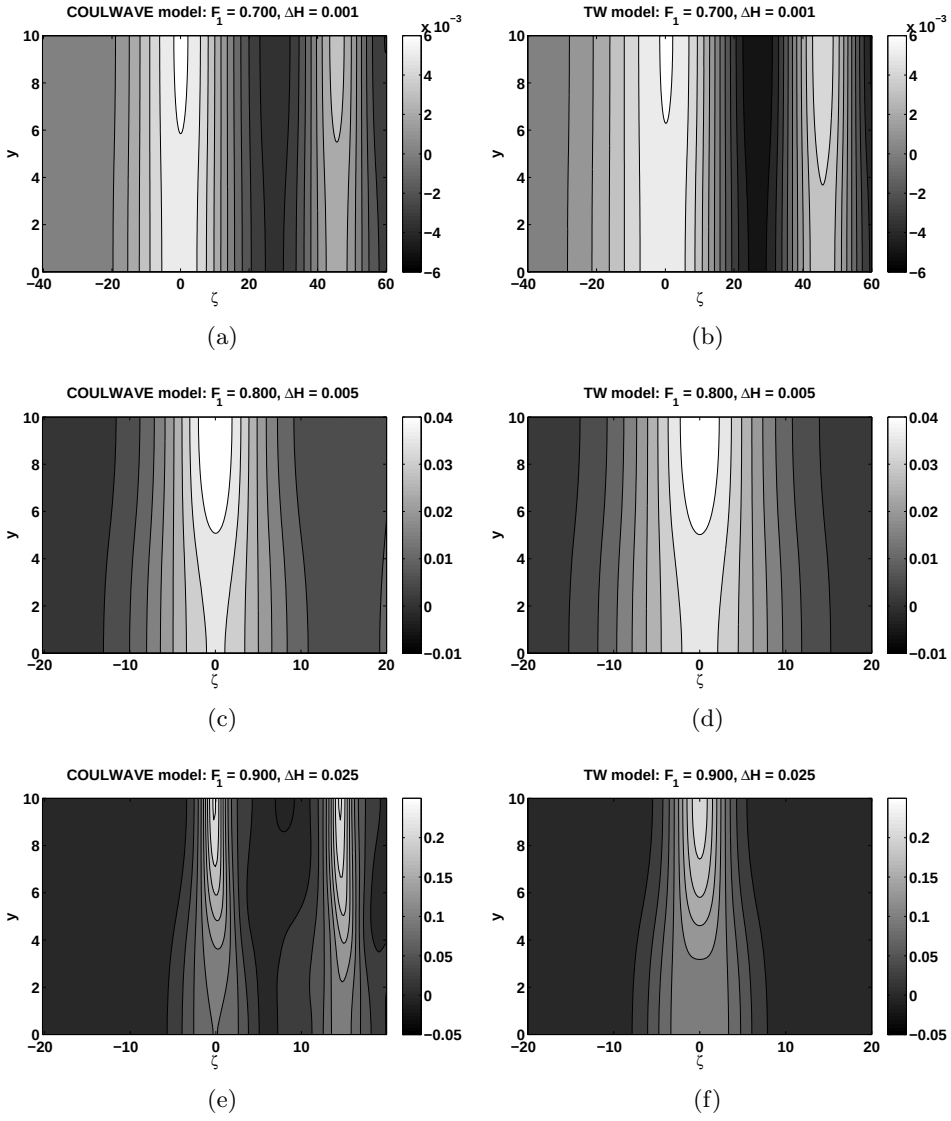

Figure 7: Comparison between TW and COULWAVE models.

the appendix.

Figure 7 shows a comparison between the leading upstream wave at $\zeta = \xi - \overline{\xi}_w$, found in the simulations with the COULWAVE model, and wave solutions from the Teng-Wu (TW) cross-channel averaged model. For $F_1 = 0.7$, it is appropriate to compare the simulated result in figure 7(a) with the Airy function, which is the solution in the linearized TW model. In the simulated result, the leading wave has a steeper wave front and the trailing waves are smaller than for the TW model result based on the Airy function. This may be due to nonlinear effects, which are small but not negligible for these waves. There is however a good agreement between the models on the cross-channel amplitude variation, which deviates by approximately $\pm 1.2\%$ at the centre line and at the channel wall. The results for $F_1 = 0.8$ and $F_1 = 0.9$ are compared to the corresponding solitary wave solution of TW with the same mean amplitude. Results for $F_1 = 0.8$, shown in figures 7(c) and 7(d), are in reasonable agreement. The cross-channel

variation in amplitude is smaller than for the COULWAVE model, resulting in a deviation between the amplitudes of approximately $\pm 2.5\%$ at the center line and at the channel wall. The wave crest of the TW solitary wave is also broader than the wave crest in the COULWAVE model. For $F_1 = 0.9$, the TW solitary wave solution is not in agreement with the COULWAVE result. The leading wave in the COULWAVE simulation has a wave length that is comparable with the channel width, and is therefor influenced by the cross-channel depth variation. Because of the short wave length, it may also be influenced by the waves following in the wave train. These results show that cross-channel averaged theory may be applicable for small amplitude solitary waves propagating in channels with a variable cross-section topography, but only if the wave length is large compared to the channel width.

Figure 7 shows the comparison between the solitary wave solution from the Teng-Wu (TW) cross-channel averaged model and the leading upstream wave at $\zeta = \xi - \overline{\xi}_w$, found in the simulations with the COULWAVE model. The best match is achieved for $F_1 = 0.8$, shown in figures 7(c) and 7(d). The cross-channel variation in amplitude is smaller than for the COULWAVE model, resulting in a deviation between the amplitudes of approximately $\pm 2.5\%$ at the center line and at the channel wall. The wave crest of the TW solitary wave is also broader than the wave crest in the COULWAVE model. For $F_1 = 0.7$, the amplitude deviation is approximately $\pm 2.1\%$ at the center line and channel wall, but now the wave length of the TW solitary wave is significantly longer than the leading wave in the COULWAVE model. This result is consistent with our previous assertion that the upstream wave behaves like an Airy function, and does not develop independent solitary waves. For $F_1 = 0.9$, the TW solitary wave solution is not in agreement with the COULWAVE result. The leading wave in the COULWAVE simulation has a wave length that is comparable with the channel width, and is therefor influenced by the cross-channel depth variation. Because of the short wave length, it may also be influenced by the waves following in the wave train. These results show that cross-channel averaged theory may be applicable for small amplitude solitary waves propagating in channels with a variable cross-section topography, but only if the wave length is large compared to the channel width.

3.3 Amplification in the wake wave pattern

Wave amplification due to wave-wave interaction can sometimes occur in the downstream wave pattern, as seen in figure 3(b). The strongest amplification is located at approximately $\xi = 10$ and $y = 7$, where the first reflected wave in the downstream wave packet interacts with the second downstream wave. A similar feature is present at approximately $\xi = 35$. A time sequence of the downstream wave pattern is shown in figure 8, and the temporal development of the amplitude of the leading downstream wave at $y = 7$ and the two leading waves at $y = 10$ is shown in figure 9. At first, the wave amplification grows with increasing amplitude of the reflected leading wave, as seen in figure 8(a). The amplitude of the leading wave peaks at approximately $t = 340$, attaining an amplitude of $\eta = 0.157$ at the channel wall, and steadily declines after this time. The amplitude of the wave at $y = 7$ continues to increase as the second downstream wave grows large. Due to the decreasing amplitude of the leading wave, the amplified wave at $y = 7$ can not be sustained indefinitely, and the amplitude decreases significantly after $t = 1500$.

Amplification due to wave-wave interaction has been found in test cases with a slightly different depth profile ($W = (4, 2, 4)$), and with different velocity of the pressure disturbance ($F_1 = 0.9$, $W = (6, 2, 2)$), as seen in figure 10. It is not clear at this point whether these amplified waves will always be transient, or if they can occur in the wave pattern after a steady state

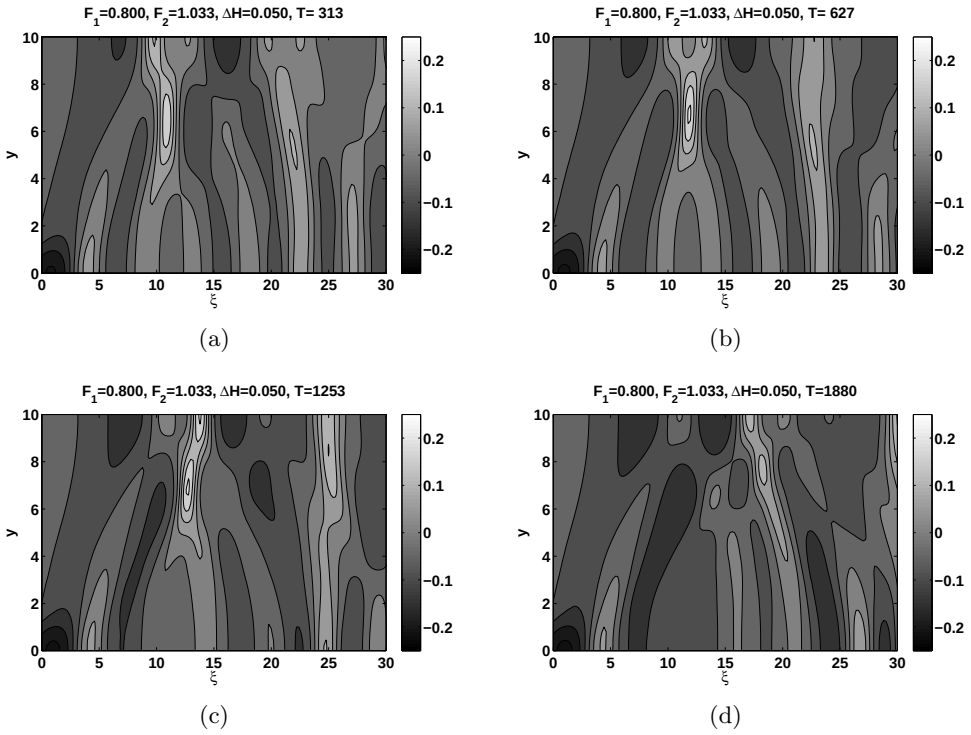

Figure 8: Wave amplification on the shallow bank due to wave-wave interaction

has been attained. Wave amplification due to wave-wave interaction has also been observed in channels with a rectangular cross-section profile, where the waves were generated by two pressure patches of equal size in a configuration resembling the hull of a catamaran, indicating that a cross-channel depth variation is not a necessary condition for this phenomenon. A similar phenomenon has been discussed by Peterson et al.[20], who studied extreme waves occurring in the intersection of two solitary wave groups. Peterson et al.[20] suggested that such a phenomenon could occur as a result of wave-wave interaction between waves from different high speed vessels, or waves from a single high speed vessel changing its direction of travel.

As mentioned earlier, the model equations reproduce the linear dispersive properties of waves in the range $0 < kh \leq \pi$. However, [11] showed that the accuracy of these equations with respect to nonlinear properties degraded sooner than the linear properties. It could therefore be questioned whether the fairly short, steep waves in the downstream wave pattern was well represented in the model. [9] explored the possibility of using 2 vertical layers to represent the flow, and found that the resulting set of equations faithfully reproduced the linear and second-order nonlinear behavior up to $kh \approx 6$. Fig. 11 shows a comparison between results for the 1-layer and 2-layer versions of the COULWAVE model corresponding to the situation in Fig. 8(b). There is a slight phase difference between the results, which becomes more apparent far downstream of the pressure patch, and the difference in maximum amplitude is approximately 4%, but the downstream wave amplification is clearly maintained also in the 2-layer model.

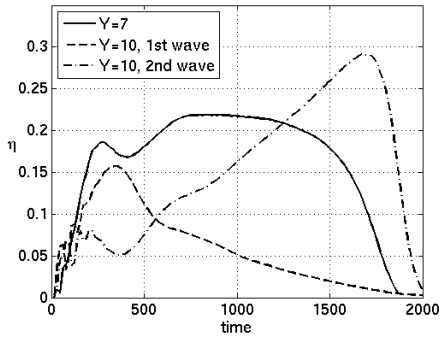

Figure 9: Time development of wave amplification on the shallow bank.

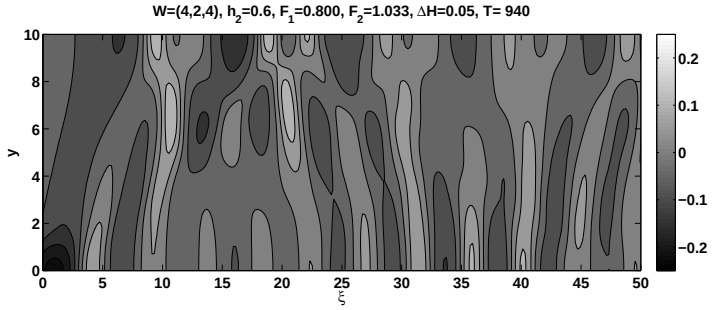

(a)

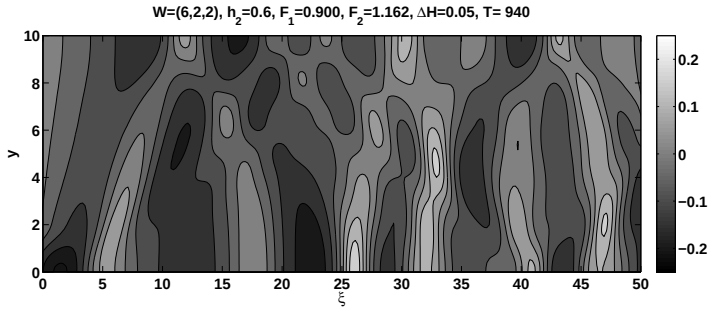

(b)

Figure 10: Wave amplification due to wave-wave interaction for different Froude numbers and channel profiles. Time of output at $t = 940$, with contour levels of $\Delta H = 0.05$.

3.4 Results for different channel parameters

In this section we consider how changes in the channel width parameters $W = (W_1, W_2, W_3)$, and channel depth parameter h_2 (keeping $h_1 = 1$), influences the wave pattern. In all these simulations we have maintained the Froude number at the trench constant at $F_1 = 0.8$. Figure 12 show wave cuts along the channel for five test cases. Figure 12(a) corresponds to the case described earlier, with $W = (3, 2, 5)$, and $h_2 = 0.6$. In figures 12(b) and 12(d) the depth h_2 is changed to 0.5 and 0.8, respectively, while maintaining the same values for W_1, W_2 and W_3 as in figure 12(a). In figure 12(c) the widths are $W = (1, 2, 7)$, and in figure 12(e) the widths are

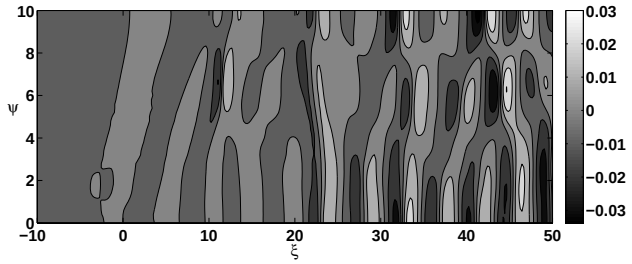

Figure 11: Comparison between simulations using 1 and 2 vertical layers: $\eta_{1-layer} - \eta_{2-layer}$. Results corresponds to Fig. 8(b) for $t = 627$.

$W = (6, 2, 2)$, and the depths h_1 and h_2 are the same as in figure 12(a).

The variation in the wave pattern displayed in these results clearly depend both on the width mean Froude number

$$\overline{F} = \frac{1}{W} \int_0^W F(y)\, dy\,,$$

and on the channel configuration. Table 1 shows the width mean Froude number and the width mean wave amplitude of the leading upstream wave for the five plots in figure 12. Although the

Constant $W = (3, 2, 5)$			Constant $h_2 = 0.6$		
h_2	$\overline{F}$	$\overline{\eta_{max}}$	W	$\overline{F}$	$\overline{\eta_{max}}$
0.45	1.0273	0.0816	$(0, 2, 8)$	1.0048	0.1249
$0.50^{12(b)}$	0.9927	0.0648	$(1, 2, 7)^{12(c)}$	0.9820	0.1002
0.55	0.9627	0.0512	$(2, 2, 6)$	0.9592	0.0676
$0.60^{4(b)}$	0.9364	0.0400	$(3, 2, 5)^{4(b)}$	0.9364	0.0400
0.65	0.9130	0.0312	$(4, 2, 4)$	0.9135	0.0249
0.70	0.8921	0.0248	$(5, 2, 3)$	0.8907	0.0174
0.75	0.8732	0.0202	$(6, 2, 2)^{12(e)}$	0.8679	0.0136
$0.80^{12(d)}$	0.8560	0.0170	$(7, 2, 1)$	0.8451	0.0118
0.85	0.8402	0.0146	$(8, 2, 0)$	0.8222	0.0108
0.90	0.8258	0.0127			
1.00	0.8000	0.0097	$(10, 0, 0)$	0.8000	0.0097

Table 1: Table of channel parameters used in Fig. 13, the corresponding width-mean Froude number, and the amplitude of the leading upstream wave. When wave profiles are shown for a particular set of channel parameters, superscripts indicate the figure number.

increase in wave amplitude near critical $\overline{F}$ resemble the results from similar tests for channels with rectangular cross-channel profiles, the magnitude of the wave amplitude and the wave period is influenced by the depth variation, as seen in figures 12(b) and 12(c). The influence of the channel configuration is seen more clearly in figure 13, where the amplitude of the leading upstream wave is plotted as a function of the width mean Froude number. These results suggest that at a given value of $\overline{F}$, the largest upstream waves will be generated in the channel with the most narrow trench.

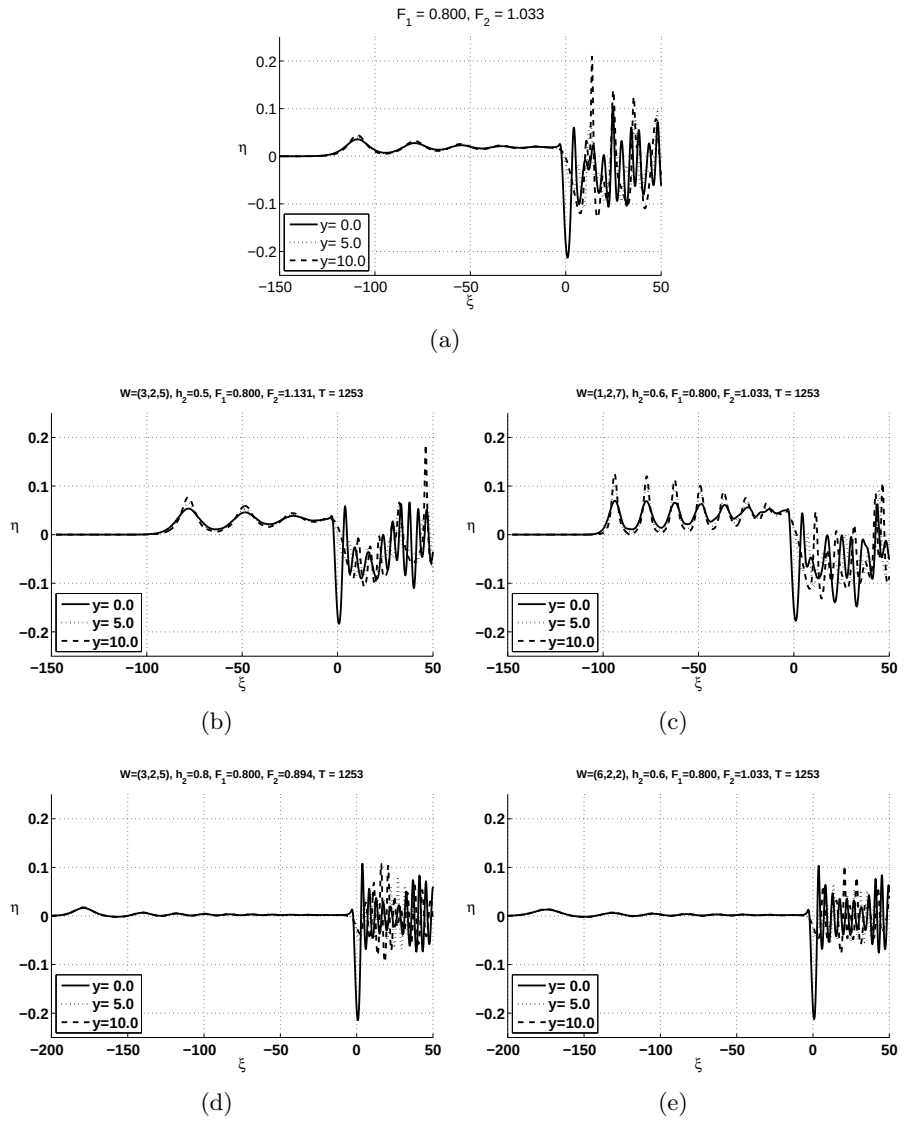

Figure 12: Waves generated for various channel width and depth parameters given in Tab. 1. Wave cuts along the channel at $t = 1253$.

3.5 Effect of an initial acceleration

Jiang et al. discuss the sensitivity of the results to the starting condition, and conclude that different initial accelerations yield different results. In our simulations the pressure disturbance accelerates from rest to the designated speed over a single time step. In figure 14 we compare results for the abruptly started pressure propagation with results where the pressure disturbance accelerates from rest over a time T. Results are shown for a later time in the acceleration case than in the abrupt start case, to compensate for the delay in the generation of upstream waves in the former case.

Differences between the results are clearly visible for $F_1 = 0.7$, where the upstream wave generation is transient in nature. A slight deviation is also visible in the upstream waves for

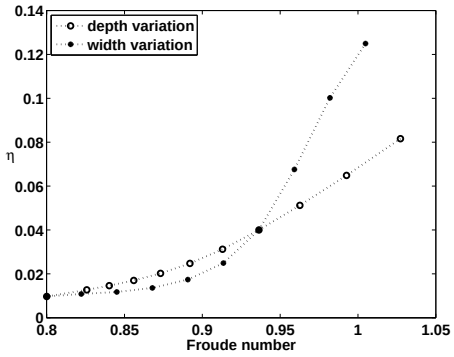

Figure 13: Amplitude of the leading upstream wave for the various for various channel width and depth parameters given in Tab. 1. Open circles signify Froude number variation due to variation of h_2. Dots signify Froude number variation due to variation of the width parameter W.

$F_1 = 0.8$, but the deviations clearly diminish with increasing F_1. We therefore conclude that the deviations due to the starting condition mainly influences the transient wave phenomena, and to lesser extent the wave pattern attained after long times.

4 Concluding remarks

In the preceding section we presented results for wave generation and propagation in a channel with a variable cross-channel topography. A case study for a similar channel configuration have previously been presented by [2] for $F_1 = 1.0$. In figure 3(c) in [2] we clearly see a wave propagating upstream of the wave-generating disturbance. Our result for $F_1 = 1.0$ and $p_a = 0.1$, seen in fig. 3(d), does not indicate upstream wave propagation. We do however find waves propagating upstream of the pressure disturbance if we run the simulation with $p_a = 0.15$, as seen in Fig. 15.

Wave generation obviously depends on both the Froude number and the magnitude of the pressure patch. In channels with a uniform cross-section topography, the latter effect is often represented in terms of the blockage coefficient; the ratio of the maximum cross-section ship area to the cross-section channel area (see e.g. [3]). In wide channels where the wave pattern displays significant cross-channel variation, Mach reflection is seen to be crucial for the generation of straight crested upstream solitary waves. Mach reflection was analyzed by [13, 14], who found that a Mach stem could be formed if $\psi_i/\sqrt{3a_i} \leq 1$, where a_i is the amplitude of the incident wave and ψ_i is the angle of incidence. [21] showed in a numerical study that conditions for Mach reflection was more restricted for large amplitude waves, i.e. they tended to reflect normally, but also showed by example that the limit of Mach reflection Mach reflection for $a_i = 0.3$ was $\psi_i = 37.8°$. Table 2 shows a comparison between the result of [21], and results for $p_a = 0.1$ (Fig. 3(d)) and $p_a = 0.15$ (Fig. 15) based on measurements from the figures. These results show why Mach reflection, and subsequent generation of upstream solitary waves, occur for $p_a = 0.15$ and not for $p_a = 0.1$ for the $F_1 = 1.0$ case.

Although the $p_a = 0.15$ result (Fig. 15) corresponds well with the result of [2], this particular configuration may not be physically sound. The Boussinesq equations tend to allow waves of

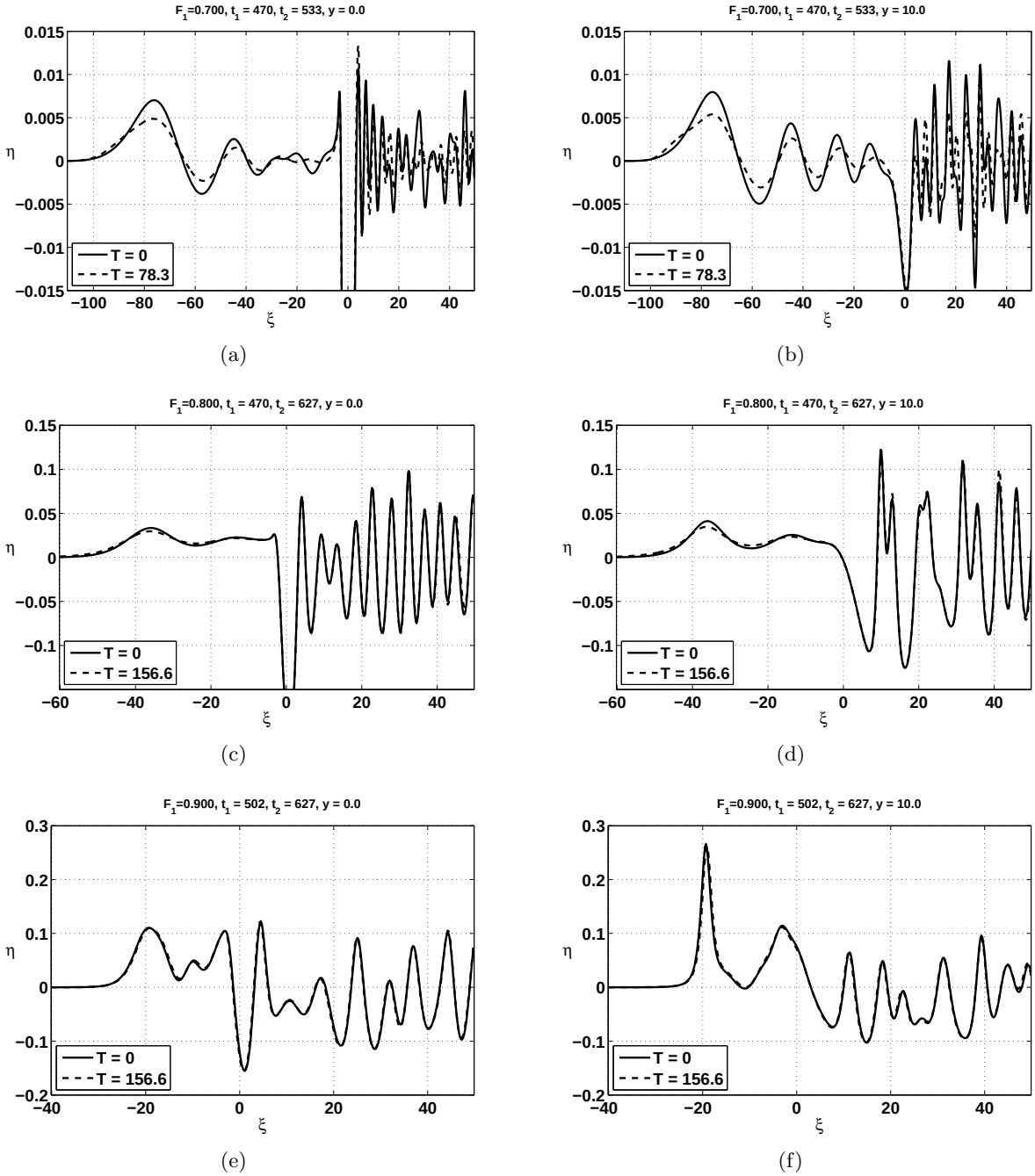

Figure 14: Comparison between results with and without acceleration from rest at the start of the simulation.

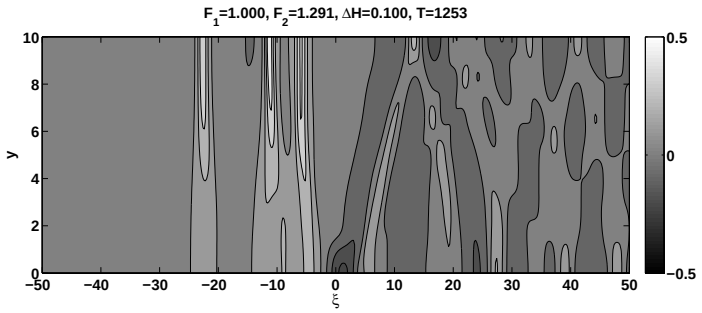

(a)

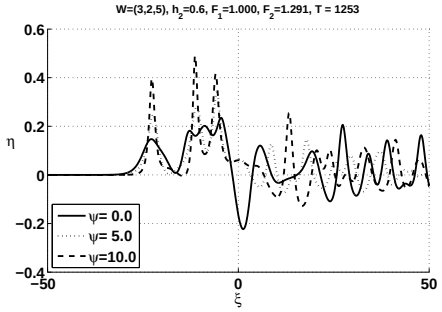

(b)

Figure 15: Wave pattern generated for $p_a = 0.15$, at Froude numbers $F_1 = 1.000$, $F_2 = 1.291$. Time of output at $t = 1253$, with contour levels of $\Delta H = 0.1$.

	a_i	ψ_i	$\psi_i/\sqrt{3a_i}$
Tanaka	0.3	37.8°	0.695
$p_a = 0.1$	0.1	50°	1.6
$p_a = 0.15$	0.25	32°	0.65

Table 2: Parameters for Mach reflection for $F_1 = 1.0$, comparing the limit value found by [21] for $a_i = 0.3$ with results for $p_a = 0.1$ and $p_a = 0.15$.

unreasonably large amplitudes and wave speeds, when in reality instabilities will cause these waves to undergo wave breaking. The upstream wave in Fig. 15 propagates at a speed of $c_w/\sqrt{h_2} = 1.32$ relative to the local shallow water wave speed near the channel wall, which exceeds the largest possible wave speed, $c_w/c_0 = 1.294$, for the solitary wave solution (see e.g. [15]). It is therefore doubtful if the simulated result, with respect to the maximum wave height, corresponds to a physically reasonable solution.

In this paper we have studied the wave generation and propagation in a channel with a variable cross-channel topography. We have found that waves may propagate upstream of the wave generating disturbance, and that the crest of these waves will span across the channel in a nearly straight line despite the variation in depth across the channel. The wave amplitude and generation time varies with the width-averaged Froude number $\overline{F}$, but is not governed by this parameter alone, as different configurations of widths and depths may result in different wave patterns for the same value of $\overline{F}$. We have also found that wave amplification may occur due to wave-wave interaction in the downstream wave packet,and can be maintained over long times. Although the variation in cross-channel topography seems to facilitate wave amplification, this does not seem to be a necessary condition for the occurrence of this phenomenon.

Acknowledgements

This work has received support from the Research Council of Norway through a grant to the program "Modelling of currents and waves for sea structures". We are indebted to Patrick Lynett for providing us with the latest version of the COULWAVE model, and to Philip L.-F. Liu and Tso-Ren Wu for guidance on how to use the model.

Appendix

In the TW model, the along channel wave propagation is computed by using a width averaged long wave model, such as the channel-Boussinesq model

$$2b\frac{\partial\tilde{\zeta}}{\partial t} + \frac{\partial}{\partial x}\left[2b(\tilde{h}+\tilde{\zeta})\bar{u}\right] = 0\,,$$
$$\frac{\partial\bar{u}}{\partial t} + \bar{u}\frac{\partial\bar{u}}{\partial x} + \frac{\partial\tilde{\zeta}}{\partial x} - \frac{1}{3}\kappa^2\tilde{h}^2\frac{\partial^3\bar{u}}{\partial x^2\partial t} = -\frac{\partial\tilde{p}_a}{\partial x}\,,$$

or the channel-KdV model

$$\frac{1}{c_0}\frac{\partial\tilde{\zeta}}{\partial t} + \left(1+\frac{3\tilde{\zeta}}{2\tilde{h}}\right)\frac{\partial\tilde{\zeta}}{\partial x} + \frac{1}{6}\kappa^2\tilde{h}^2\frac{\partial^3\tilde{\zeta}}{\partial x^3} + \left(\frac{1}{4\tilde{h}}\frac{\partial\tilde{h}}{\partial x} + \frac{1}{2b}\frac{\partial b}{\partial x}\right) = -\frac{1}{2}\frac{\partial\tilde{p}_a}{\partial x}\,,$$

where $c_0 = (g\tilde{h})^{\frac{1}{2}}$ is a characteristic speed, and the *shape factor* κ^2 is determined by the channel geometry (see e.g. Teng and Wu[22, 23, 24]). Width averages and cross section averages are computed by

$$(\tilde{\cdot}) = \frac{1}{2b}\int_{-b}^{b}(\cdot)\,dy\,,$$
$$(\bar{\cdot}) = \frac{1}{A_0}\iint_{A_0}(\cdot)\,dy\,dz\,,$$

where $2b$ is the channel width at $z = 0$ and A_0 is the equilibrium area of the cross section. The general formulation allows b to vary in the along-channel direction, but we have only used a constant value for b in our applications. The cross channel perturbation is found by solving the Poisson equation with boundary conditions

$$\begin{aligned} \Psi_{yy} + \Psi_{zz} &= 1\,, \\ \Psi_z|_{z=0} &= \tilde{h}\,, \quad \text{(at the frees surface)}\,, \\ \Psi_n &= 0\,, \quad \text{(at channel walls below the} \\ &\qquad \text{unperturbed water surface)}\,, \end{aligned}$$

where n is the unit normal vector at the solid boundaries. This determines the shape factor

$$\kappa^2 = \frac{3}{\tilde{h}}(\tilde{\Psi} - \bar{\Psi})\,.$$

The width averaged solitary wave solution with amplitude α is

$$\tilde{\zeta} = \alpha\,\mathrm{sech}^2\sqrt{\frac{3\alpha}{4\kappa^2}}(x - ct)\,,$$

and the width averaged solution to the linearized problem can be written in terms of the Airy function Ai as

$$\tilde{\zeta} = \beta\left(\tfrac{1}{2}\kappa^2\tilde{h}^2 t\right)^{-\frac{1}{3}} Ai\left[-x\left(\tfrac{1}{2}\kappa^2\tilde{h}^2 t\right)^{-\frac{1}{3}}\right]\,,$$

where β determines the wave amplitude. The wave profile including cross channel effects is

$$\zeta(x, y, t) = \tilde{\zeta}(x, t) - (\Psi|_{z=0} - \tilde{\Psi})\tilde{\zeta}_{xx}$$

The problem outlined above has been solved using the Poisson solver included in MATLAB.

References

[1] R. C. Ertekin, W. C. Webster, and J. V. Wehausen. Waves caused by a moving disturbance in a shallow channel of finite width. *J. Fluid Mech.*, 169:275–292, 1986.

[2] T. Jiang, R. Henn, and S. D. Sharma. Wash waves generated by ships moving on fairways of varying topography. In *Proceedings for the 24th Symposium on Naval Hydrodynamics*, Fukuoka, 2002.

[3] C. Katsis and T. R. Akylas. On the exitation of long nonlinear water waves by a moving pressure distribution. part 2. three-dimensional effects. *J. Fluid Mech.*, 177:49–65, 1987.

[4] Y. Li and P. D. Sclavounos. Three-dimensional nonlinear solitary waves in shallow water generated by an advancing disturbance. *J. Fluid Mech.*, 470:383–410, 2002.

[5] P. L.-F. Liu. Model equations for wave propagation from deep to shallow water. *Adv. Coastal Engng.*, 1:125–157, 1994.

[6] P. L.-F. Liu and T.-R. Wu. Waves generated by moving pressure disturbances in rectangular and trapezoidal channels. *Journal of Hydraulic Research*, 42(2):163–171, 2004.

[7] P. Lynett and P. L.-F. Liu. Coulwave model page: Modeling wave generation, evolution, and interaction with depth-integrated, dispersive wave equations. http://ceprofs.tamu.edu/plynett/COULWAVE/.

[8] P. Lynett and P. L.-F. Liu. A numerical study of submarine landslide generated waves and runup. *Royal Society of London A*, 458(2028):2885–2910, 2002.

[9] P. Lynett and P. L.-F. Liu. A two-layer approach to wave modelling. *Proc. R. Soc. Lond. A*, 460(2049):2637–2669, 2004.

[10] P. Lynett, T.-R. Wu, and P. L.-F. Liu. Modeling wave runup with depth-integrated equations. *Coast. Engrg.*, 46(2):89–107, 2002.

[11] P. A. Madsen and H. A. Schäffer. Higher-order boussinesq-type equations for surface gravity waves: Derivation and analysis. *Phil. Trans. R. Soc. Lond. A*, 356:3123–3184, 1998.

[12] J. Mathew and T. R. Akylas. On three-dimensional long water waves in a channel with sloping sidewalls. *J. Fluid Mech.*, 215:289–307, 1990.

[13] J. W. Miles. Obliquely interacting solitary waves. *J. Fluid Mech.*, 79(1):157–169, 1977.

[14] J. W. Miles. Resonantly interacting solitary waves. *J. Fluid Mech.*, 79(1):171–179, 1977.

[15] J. W. Miles. Solitary waves. *Ann. Rev. Fluid Mech.*, 12:11–43, 1980.

[16] O. Nwogu. Alternative form of boussinesq equations for nearshore wave propagation. *Journal of waterway, port, coastal, and ocean engineering*, 119(6):618–638, 1993.

[17] G. Pedersen. Three-dimensional wave patterns generated by moving disturbances at transcritical speeds. *J. Fluid Mech.*, 196:39–63, 1988.

[18] D. H. Peregrine. Long waves in a uniform channel of arbitrary cross-section. *J. Fluid Mech.*, 32(2):353–365, 1968.

[19] A. S. Peters. Rotational and irrotational solitary waves in a channel with arbitrary cross-section. *Commun. pure appl. Math*, 19:445–471, 1966.

[20] P Peterson, T Soomere, J Engelbrecht, and E. van Groesen. Soliton interaction as a possible model for extreme waves in shallow water. *Nonlinear Processes in Geophysics*, 10:503–510, 2003.

[21] M. Tanaka. Mach reflection of a large-amplitude solitary wave. *J. Fluid Mech.*, 248:637–661, 1993.

[22] M. H. Teng and T. Y. Wu. Nonlinear water waves in channels of arbitreary shape. *J. Fluid Mech.*, 242:211–233, 1992.

[23] M. H. Teng and T. Y. Wu. Evolution of long water waves in variable channels. *J. Fluid Mech.*, 266:303–317, 1994.

[24] M. H. Teng and T. Y. Wu. Effects of channel cross-sectional geometry on long wave generation and propagation. *Phys. Fluids*, 9(11):3368–3377, 1997.

[25] G. Wei, J. T. Kirby, S. T. Grilli, and R. Subramanya. A fully nonlinear boussinesq model for surface waves. part 1. highly nonlinear unsteady waves. *Journal of Fluid Mechanics*, 294:71–92, 1995.